Macroscopic effects of isolated-attosecond-pulse generation with a temporally asymmetric laser field

Zhiyong Qin ⃝, Changhai Yu ⃝,* Jiansheng Liu,† Zhijun Zhang, Shiyi Zhou, Zibo Xu, Jintan Cai,
Xuhui Jiao, and Zhongtao Xiang

Department of Physics, Shanghai Normal University, Shanghai 200234, China

We present a theoretical investigation of an efficient method for generating macroscopic high-order harmonics with a smooth broadband continuous spectrum structure driven by a temporal asymmetric laser field. Our study demonstrates that selected continuous high-order harmonic spectra can support isolated attosecond pulses (IAPs) in the extreme ultraviolet region. Time-frequency analysis of high-order harmonics reveals that the smooth broadband continuous spectrum is dominated by long-trajectory electron emissions. The quantitative analysis of the phase mismatching reveals that the generation of the IAP is caused by the favorable transient phase matching of the long-trajectory electron emissions in the macroscopic medium, which can be attributed to the spatiotemporal reshaping of the laser waveform at high gas pressure. Furthermore, we also investigate the dependency of IAP on gas pressure and laser chirp parameters and find that the pulse width of the generated IAPs can be controlled by adjusting the gas pressure and the chirp parameters.

I. INTRODUCTION

High-order harmonic generation (HHG) produced by the interaction of intense laser pulses with a gaseous medium is a widespread technique for the generation of attosecond pulses [1–3]. The unprecedented resolution of attosecond pulses makes it possible to study ultrafast processes with extremely short timescales, such as ultrafast electronic dynamics inside atoms, molecules, and solids as well as for time-resolved surface physics [4–9]. Typically, the attosecond pulses produced in HHG processes are either attosecond pulse trains (APTs) consisting of two bursts within a laser period or isolated attosecond pulses (IAPs), depending on the experimental conditions. For most of the applications, the IAPs are preferred because they allow for direct recording of the temporal evolution of the ultrafast dynamics without side effects from the pulse trains [10]. Since the initial discovery of IAP in 2001 [3], there has been extensive research and significant progress made in generating IAPs through HHG [11,12].

The HHG process in gaseous atoms can be described by the semiclassical three-step model [13], which involves ionization, acceleration, and recombination and results in the generation of APTs every half cycle of the driving field. Therefore, the IAPs can only be obtained by limiting the efficient HHG process within half the optical cycle (o.c.) of the driving laser field [4]. So far, various gating methods have been developed to achieve this, including polarization gating for an isolated 53-as pulse [14–16], amplitude gating for an isolated 43-as pulse with passive carrier-envelope phase (CEP) stabilized midinfrared drivers [17–19], double optical gating for a 67-as pulse [20–23], and multicolor waveform gating [24–26]. Usually, these methods involve waveform

shaping of the driving laser pulse to restrict harmonic emission to a very short period. For example, in the multicolor waveform gating method, a two-color or multicolor laser field is synthesized to control the driver waveform. This approach not only breaks up the half-cycle symmetry of the attosecond pulse generation and relaxes the restrictions of the pulse duration of driving lasers but is also expected to increase the cutoff energy of the harmonics and the efficiency of IAP generation [27]. Xue *et al.* recently demonstrated a reproducible generation of an intense continuum harmonic spectrum in the soft x-ray region using a stable 50-mJ three-channel optical waveform synthesizer, resulting in pulse energies above 0.24 μJ and a transform limit duration of 170 as [28,29]. In addition, several other methods for generating IAPs have been established in recent years, including ionization gating [30–32], attosecond lighthouse [33–35], and phase-matching gating [36–38]. These methods take into account the propagation and phase matching of the HHG in the macroscopic medium for the IAP generation, where only a few parts of the harmonic emission can be coherently built up. For example, in the ionization gating method, the ionization rate in the driver pulse trailing (descending) edge is much higher than that in the pulse leading (ascending) edge, which leads to phase mismatching of the harmonics generated in the driver pulse trailing edge and suppresses harmonic emission in the macroscopic medium. This is equivalent to forming a phase-matched temporal window where the HHG process only occurs in part of the pulse leading edge [30]. Similar to ionization gating, the phase-matching gating method controls the spatiotemporal evolution of the driver pulse by the ionization process, plasma-induced defocusing, and the Kerr effect in the macroscopic medium where a time-gated phase matching [39] or a spatiotemporal wavefront rotation gating [40] can be formed for the IAP generation. Schötz *et al.* experimentally demonstrated the generation of IAPs with the center energy around 80 eV, and 324-as duration by sub-

two-cycle laser pulses at 750 nm in argon in the overdriven regime, where ionization loss and plasma dispersion strongly modify the driving laser pulse over small distances to form a transient phase matching for IAP generation [37]. Tang *et al.* demonstrated the optimal conditions for IAP generation in an overdriven ionized medium, where the spatiotemporal wavefront rotation of the driving laser can be well controlled, leading to spatially well-separated attosecond bursts in the far field, like the attosecond lighthouse technique [40].

In recent years, advances in optical pulse shaping technology have made it possible to generate an electric field with arbitrary spatiotemporal waveforms by only one laser pulse [41–43], which is promising for the HHG process such as extending the cutoff energy and generating the IAPs [44–48]. For instance, by using a chirped laser pulse the HHG cutoff energy can be significantly extended and IAPs can also be obtained with a bandwidth filter [44,49]. In addition, a spatially inhomogeneous laser field originating from the interaction between an ultrashort laser pulse and a gold nanostructure can also be used to generate ultrashort IAPs by reducing the inherent chirp of the harmonics [50,51]. The spatiotemporal shaping methods above are mainly to regulate the electron dynamics in the HHG process on the single-atom level to obtain the IAPs or extend the cutoff energy. However, as mentioned above, the HHG is an extremely nonlinear process in which all atoms in a gas medium are excited by the driving laser, and the output high-order harmonics are the macroscopic response to the generation medium. Therefore, in this paper, we propose a scheme by numerical simulations to generate IAPs based on the optical pulse shaping method and phase-matching gating. In this scheme, a temporal asymmetric laser pulse was used to interact with a helium gas medium to generate high-order harmonics. In experiments, this temporal asymmetric laser field can be formed through the self-steepening effect of the laser in a transparent medium [52,53] or the interaction of the laser with a gold ellipsoidal nanostructure [54]. In this work, the single-atom response is calculated by the strong-field approximation (SFA) model, and the macroscopic propagation of the driving laser and harmonic fields is obtained by solving the three-dimensional Maxwell's wave equations with full electric field. By using this scheme, an isolated 117-as attosecond pulse in the extreme ultraviolet region with a bandwidth of 43 eV can be obtained directly from the continuum harmonic spectrum near the cutoff energy. The simulated results show that this IAP generation is caused by the favorable transient phase matching of the long-trajectory electron emissions driven by the temporal asymmetric laser field in the macroscopic medium. The quantitative analysis of the phase mismatching shows that this transient phase matching is attributed to the spatiotemporal reshaping of the laser waveform at high gas pressure. Furthermore, the results also show that the pulse width of the generated IAPs can be controlled by adjusting the gas pressure and the chirp parameters of the driven laser.

II. THEORETICAL METHODS

A. Propagation of fundamental laser and harmonic fields

In our numerical model, the single-atom response of the harmonic radiation is calculated using the SFA, or the

so-called Lewenstein model [55]. This approach has been shown to provide good qualitative agreement with the numerical solution of the Schrödinger equation. In order to simulate the macroscopic effects of the harmonics generated in the gas medium, the propagation of the fundamental laser and harmonic fields should be considered, which can be described by Maxwell's equations. The single-atom response is inserted as a source term into the wave equations of the fundamental and the harmonic fields, which are solved in cylindrical coordinates, assuming radial symmetry. The propagation of the fundamental driving laser and the harmonic field in a gas medium is described by [56–58]

$$\nabla^2 E_1(r,z,t) - \frac{1}{c^2}\frac{\partial^2 E_1(r,z,t)}{\partial t^2}$$
$$= \mu_0 \frac{\partial J_{abs}(r,z,t)}{\partial t} + \frac{\omega_0^2}{c^2}\big(1 - \eta_{eff}^2\big)E_1(r,z,t), \quad (1)$$

$$\nabla^2 E_h(r,z,t) - \frac{1}{c^2}\frac{\partial^2 E_h(r,z,t)}{\partial t^2} = \mu_0 \frac{\partial^2 P(r,z,t)}{\partial t^2}, \quad (2)$$

where $E_1(r,z,t)$ and $E_h(r,z,t)$ are the electric field of the fundamental laser pulse with central frequency ω_0 and the harmonic field, respectively, and z is the axial propagation direction. The propagation of the fundamental driving laser is affected by refraction, nonlinear self-focusing, ionization, and plasma defocusing. The effective refractive index η_{eff} of the gas medium is given by

$$\eta_{eff}(r,z,t) = \eta_0(r,z,t) + \eta_2 I(r,z,t) - \frac{\omega_p^2(r,z,t)}{2\omega_0^2}. \quad (3)$$

Here, the first term $\eta_0 = 1 + \delta_1 - i\beta_1$ includes refraction effect δ_1 and absorption effect β_1 of neutral atoms. In general, the absorption effect (β_1) on the fundamental laser in the gas medium is very small and can be neglected in simulation. The second term in Eq. (3) is the optical Kerr effect which depends on the laser intensity $I(r,z,t)$, and the third term takes into account the contributions of the free electrons which contain the plasma frequency $\omega_p = [e^2 n_e(r,z,t)/(\varepsilon_0 m_e)]^{1/2}$, where m_e and e represent the mass and charge of the electron, respectively, and n_e is the density of free electrons, which can be given by the Ammosov-Delone-Krainov (ADK) ionization rate [59]. The absorption term of the ionization medium in Eq. (1) is

$$J_{abs}(r,z,t) = \frac{w(r,z,t)[n_0 - n_e(r,z,t)]I_p E_1(r,z,t)}{|E_1(r,z,t)|^2}, \quad (4)$$

where $w(t)$ is the ionization rate calculated with the ADK theory, and n_0 is the neutral atom density. Therefore, the wave equation of the fundamental laser in Eq. (1) can be written as

$$\nabla^2 E_1(r,z,t) - \frac{1}{c^2}\frac{\partial^2 E_1(r,z,t)}{\partial t^2}$$
$$= \mu_0 \frac{\partial J_{abs}(r,z,t)}{\partial t} + \frac{\omega_p^2}{c^2}E_1(r,z,t)$$
$$- 2\frac{\omega_0^2}{c^2}(\delta_1 + \eta_2 I)E_1(r,z,t). \quad (5)$$

By changing to the moving coordinate frame ($z' = z$, $t' = t - z/c$) and performing the paraxial approximation (i.e.,

neglecting the $\partial^2 E_1 / \partial z'^2$ term), we obtain the equation

$$
\nabla_\perp^2 E_1(r, z', t') - \frac{2}{c} \frac{\partial^2 E_1(r, z', t')}{\partial z' \partial t'}
$$
$$
= \mu_0 \frac{\partial J_{abs}(r, z', t')}{\partial t'} + \frac{\omega_p^2}{c^2} E_1(r, z', t')
$$
$$
- 2 \frac{\omega_0^2}{c^2} (\delta_1 + \eta_2 I) E_1(r, z', t'). \tag{6}
$$

The temporal derivative in Eq. (6) can be eliminated by a Fourier transform, yielding the equation

$$
\nabla_\perp^2 \tilde{E}_1(r, z', \omega) - \frac{2i\omega}{c} \frac{\partial \tilde{E}_1(r, z', \omega)}{\partial z'} = \tilde{G}(r, z', \omega), \tag{7}
$$

where

$$
\tilde{E}_1(r, z', \omega) = \mathcal{F}[E_1(r, z', t')], \tag{8}
$$

$$
\tilde{G}_1(r, z', \omega) = \mathcal{F}\left[\mu_0 \frac{\partial J_{abs}(r, z', t')}{\partial t'} + \frac{\omega_p^2}{c^2} E_1(r, z', t') \right.
$$
$$
\left. - 2 \frac{\omega_0^2}{c^2} (\delta_1 + \eta_2 I) E_1(r, z', t') \right], \tag{9}
$$

and $\mathcal{F}$ is the Fourier transform operator acting on the temporal coordinate. The fundamental laser field is assumed to be Gaussian both in space and in time at the entrance of a gas medium, and the pressure is assumed to be constant within the gas medium.

For the harmonic field, the source term $P(r, z, t)$ in Eq. (2) is related to the single-atom-induced dipole moment and depends upon the fundamental driving laser field $E_1(r, z, t)$. In the harmonic propagation equation, we have neglected the free-electron dispersion because the plasma frequency is much lower than the harmonics frequencies. Again, going to the moving coordinate frame and using the paraxial approximation, Eq. (2) becomes

$$
\nabla_\perp^2 E_h(r, z', t') - \frac{2}{c} \frac{\partial^2 E_h(r, z', t')}{\partial z' \partial t'} = \mu_0 \frac{\partial^2 P(r, z', t')}{\partial t'^2}. \tag{10}
$$

We also eliminate the temporal derivative by a Fourier transform and obtain the equation

$$
\nabla_\perp^2 \tilde{E}_h(r, z', \omega) - \frac{2i\omega}{c} \frac{\partial \tilde{E}_h(r, z', \omega)}{\partial z'} = -\omega^2 \mu_0 \tilde{P}(r, z', \omega), \tag{11}
$$

where

$$
\tilde{E}_h(r, z', \omega) = \mathcal{F}[E_h(r, z', t')], \tag{12}
$$

and

$$
\tilde{P}(r, z', \omega) = \mathcal{F}[P(r, z', t')]. \tag{13}
$$

The polarization term describes the response of the medium to the laser field and includes both linear and nonlinear terms $\tilde{P}(r, z', \omega) = \chi^{(1)}(\omega) \tilde{E}_h(r, z', \omega) + \tilde{P}_{nl}(r, z', \omega)$, where the linear susceptibility $\chi^{(1)}(\omega)$ includes both linear dispersion and absorption through its real and imaginary parts, respectively. The refractive index of the gas medium to the

harmonics is written as $n(\omega) = \sqrt{1 + \chi^{(1)}(\omega)/\varepsilon_0}$ and is related to atomic scattering factors by

$$
n(\omega) = 1 - \delta_h(\omega) - i\beta_h(\omega) = 1 - \frac{1}{2\pi} n_0 r_e \lambda^2 (f_1 + f_2), \tag{14}
$$

where r_e is the classical electron radius, λ is the harmonic wavelength, n_0 is the neutral atom density, and f_1 and f_2 are atomic scattering factors [60].

The nonlinear polarization term $\tilde{P}_{nl}(r, z', \omega)$ can be expressed as

$$
\tilde{P}_{nl}(r, z', \omega) = \mathcal{F}\{[n_0 - n_e(r, z', t')]D(r, z', t')\}, \tag{15}
$$

where $n_e(r, z', t')$ is the free-electron density and $D(r, z', t')$ is the single-atom-induced dipole moment calculated by the SFA model. Finally, the harmonic propagation equation becomes

$$
\nabla_\perp^2 \tilde{E}_h(r, z', \omega) - \frac{2i\omega}{c} \frac{\partial \tilde{E}_h(r, z', \omega)}{\partial z'}
$$
$$
- \frac{2\omega^2}{c^2} [\delta_h(\omega) + i\beta_h(\omega)] \tilde{E}_h(r, z', \omega)
$$
$$
= -\omega^2 \mu_0 \tilde{P}_{nl}(r, z', \omega). \tag{16}
$$

After the propagation in the medium, we obtain the harmonics fields at the exit face of the gas medium. Note that $\delta_h(\omega)$ and $\beta_h(\omega)$ in Eq. (16) account for the dispersion and absorption of the medium on the harmonics, respectively. Equations (7) and (16) can be solved using the Crank-Nicolson method [57].

B. Time-frequency analysis

The total harmonic power spectra at different positions in the gas medium can be obtained by integrating over the radial direction [61],

$$
S_h(z', \omega) \propto \int_0^\infty 2\pi r |\tilde{E}_h(r, z', \omega)|^2 dr, \tag{17}
$$

where $\tilde{E}_h$ is the Fourier transform of the harmonic field E_h. Attosecond pulses at different positions can be calculated by superimposing HHG in a certain frequency range [62]:

$$
I_h(z', t) = \int_0^\infty 2\pi r dr \left| \int_{\omega_1}^{\omega_2} \tilde{E}_h(r, z', \omega) e^{i\omega t} d\omega \right|^2. \tag{18}
$$

The time-frequency representation of the harmonic field $E_h(r, z', t')$ is a simultaneous representation of the temporal and spectral characteristics of the harmonics. We perform the time-frequency analysis in terms of the wavelet transform of the harmonic field,

$$
A(z', t, \omega) = \int E_h(r, z', t') w_{t,\omega}(t') dt', \tag{19}
$$

with the wavelet kernel $w_{t,\omega}(t') = \sqrt{\omega} W[\omega(t - t')]$, where the $W(x)$ is the Morlet wavelet [62,63]. The width of the window function in the wavelet transform varies as the frequency changes. In order to avoid the complexity of the harmonic spatial distribution, we calculate the wavelet analysis for each radial point at different positions in the gas medium and then

integrate it over the radial coordinate:

$$|A(z',t,\omega)|^2 = \int_0^{\infty} 2\pi r dr \left| \int E_h(r,z',t') w_{t,\omega}(t') dt' \right|^2. \quad (20)$$

C. Time-dependent phase matching

The above theoretical model is sufficient to simulate the HHG in a macroscopic medium, while for deeper insight into the underlying physical mechanism, the phase matching of the HHG should be investigated. Phase matching refers to the constructive accumulation of radiation from coherent sources along the beam propagation direction. An optimum phase matching of the qth harmonic in the HHG process is $k_q = qk_1$, where k_q is the qth harmonic wave vector and k_1 is the fundamental laser wave vector. Since the HHG is an extremely nonlinear process, both the single-atom response and the macroscopic effects could cause the phase mismatching of the harmonics. Usually, the phase mismatching degree of the qth harmonic can be expressed as [64,65]

$$\Delta k_q = k_q - qk_1 = \Delta k_d + \Delta k_n + \Delta k_p + \Delta k_g. \quad (21)$$

Here $\Delta k_d(z,t) = -\alpha_j \nabla I(z,t)$ is the intrinsic harmonic dipole phase mismatching induced by the intensity-dependent trajectories in single-atom response, where α_j is a coefficient related to the electron trajectories with $j = S, L$ representing the short and long paths. $\Delta k_n(z,t) = 2\pi q P(z)[1-p(z,t)]\Delta n/\lambda$ and $\Delta k_p(z,t) = -P(z)N_{\text{atm}}p(z,t)r_e\lambda(q^2-1)/q$ are the phase mismatching due to the dispersion of the neutral atomic and free electrons, respectively, in which $P(z)$ is the gas pressure and $p(z,t)$ is the ionization probability, Δn is the refractive index difference per atmosphere between the qth harmonic and the drive laser with wavelength λ, and N_{atm} is the initial atomic number density per atmosphere. Lastly, $\Delta k_g(z,t) = q\nabla\Phi_g(z,t)$ is the phase mismatching arising from the Gouy phase shift $\Phi_g(z,t)$, resulting from the geometrical focusing of the drive laser beam.

III. RESULTS AND DISCUSSION

A. Macroscopic HHG spectra and IAPs at the exit of the gas medium

In our simulations, we adopt an 800-nm laser field with a peak intensity of 8×10^{14} W/cm^2 and a laser beam waist of 35 μm. The laser field is expressed as $E(t) = E_0 f(t)\cos(\omega t)$, where the time envelope function in the asymmetric and symmetric pulse is expressed as

$$f(t) = \begin{cases} e^{-2\ln 2 \frac{t^2}{\tau_1^2}} (t < 0) + e^{-2\ln 2 \frac{t^2}{\tau_2^2}} (t \geqslant 0) & \text{for asymmetric pulse} \\ e^{-2\ln 2 \frac{t^2}{\tau_0^2}} & \text{for symmetric pulse} \end{cases}. \quad (22)$$

Here $\tau_1 = 5T_0$ and $\tau_2 = 1T_0$ are the pulse width of the leading edge and trailing edge in the asymmetric pulse, $\tau_0 = 3T_0$ is the pulse width in the symmetric pulse, and T_0 is the o.c. of the laser pulse. It can be seen that both laser pulses have the same pulse duration which at full width at half maximum (FWHM) is about 8 fs. The laser pulse is focused at the center of the helium gas target, and the length of the medium is 1.2 mm with a uniform gas pressure distribution. Figure 1(a) shows the laser envelope in the asymmetric (solid red line) and the symmetric (dashed blue line) pulse; the corresponding ionization probability in both laser pulses is shown in Fig. 1(b). Although both the asymmetric and symmetric pulses have different envelopes, their maximum ionization probability is nearly the same, which is 1.45% and 1.4%, respectively.

To investigate the macroscopic process of the HHG driving by both kinds of laser pulses, the gas pressure was chosen to be 900 Torr, and the results are shown in Fig. 2. Figure 2(a) shows the macroscopic HHG spectra power at the exit of the gas medium driving by the asymmetric (red line) and symmetric (blue dashed line) laser pulse. Although the HHG spectra in both cases are similar to each other and have the same cutoff harmonic order 110 (H110), the HHG spectra in the region from H56 to H84 (43 eV) exhibit a smooth continuous broadband spectrum structure in the case of the asymmetric pulse. The broadband spectrally continuous harmonics usually indicate an IAP in the time domain. To check whether IAPs exist driven by the two kinds of laser pulses, we synthesized the high-order harmonics from H56 to H84

in both cases in Fig. 2(a) to obtain the attosecond pulses, and the result is shown in Fig. 2(b). It can be seen that on the macroscopic level, the HHG driving by the asymmetric laser pulse exhibits an IAP in the time domain with relatively high intensity and a shortest pulse duration of 117 as (red line) near $-0.1T_0$, but the harmonics generated by the
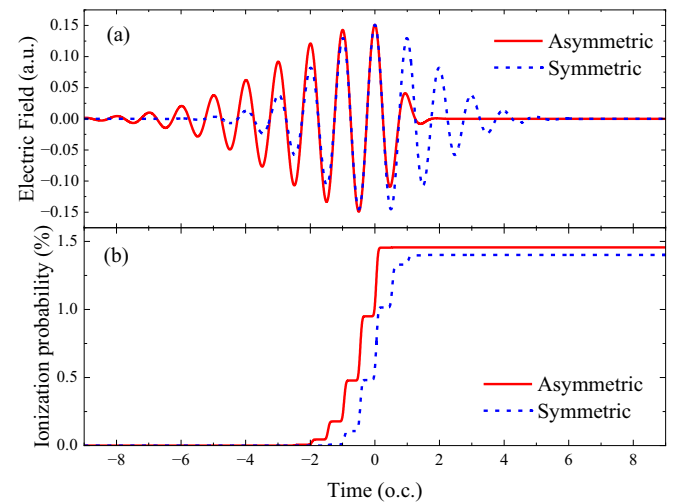

FIG. 1. (a) The envelope of the laser field with asymmetric (solid red line) and symmetric pulses (dashed blue line). (b) The corresponding ionization probability with time.
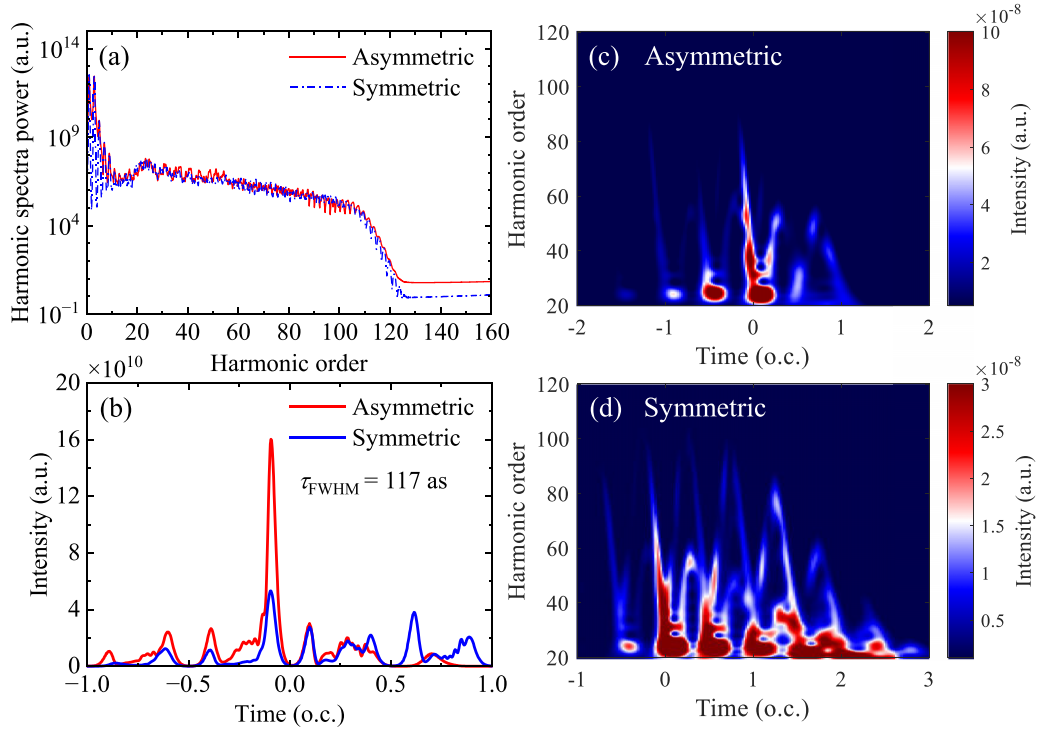
FIG. 2. (a) Macroscopic HHG spectra power generated by the asymmetric (red line) and symmetric (blue dashed line) pulses in 900 Torr helium gas. Each harmonic spectrum is obtained by integrating the harmonic yields over radial distance at the exit plane of the gas medium. (b) Attosecond pulses are obtained by superimposing selected high-order harmonics (H56–H84) in (a) generated by the asymmetric [red (upper) line] and symmetric [blue (lower) line] laser pulses. (c), (d) Time-frequency analysis of near-field HHG at the exit plane of the gas medium driven by the two kinds of laser pulses.

symmetric pulse exhibit APTs with lower intensity (blue line). For a better understanding of the emission features of the harmonics in Fig. 2(a), we examined the time-frequency analysis of the integrated harmonics on the exit plane of the gas medium perpendicular to the propagation direction under the two kinds of laser pulses, as shown in Figs. 2(c)–2(d). Compared with the harmonic emissions driven by the symmetric pulse which has an attosecond burst in every half o.c., the harmonics above H60 generated in the case of an asymmetric laser pulse have only one strong attosecond burst between $-2T_0$ and $2T_0$, which locates around $-0.1T_0$. Furthermore, the attosecond burst in the asymmetric pulse has only one major emission branch with the negative chirp, as shown in Fig. 2(c), which results from the long electron trajectories. However, the attosecond bursts in the case of a symmetric pulse have two branches and the long-trajectory branch is slightly stronger than the short-trajectory one, as shown in Fig. 2(d).

In order to further clarify the contributions of long and short electron trajectories to each order of harmonic emission in the case of the symmetric laser pulse, Fig. 3(a) shows the time-dependent emission intensity of a given harmonic order ranging from H56 to H84. The results show that the harmonic emission in the range of $-0.4T_0$ to $-0.2T_0$ is suppressed, while the harmonic emission in the range of $-0.2T_0$ to $0T_0$ is enhanced and relatively concentrated around $-0.1T_0$; this is in agreement with the results in Fig. 2(c) that the attosecond burst has only one major emission branch which is

produced by the long electron trajectories. To investigate the spatial distribution of the attosecond pulses in the two kinds of laser pulses, we superimposed the high-order harmonics from H56 to H84 in each radial position on the exit plane of the gas medium, as shown in Figs. 3(c) and 3(d), respectively. It can be seen that in both kinds of laser pulses, the generated attosecond pulses are mainly concentrated within the 0–10-μm region in the radial direction. Moreover, in the case of the asymmetric pulse, the generated harmonics exhibit IAPs in the time domain in the entire 10-μm radial region and are concentrated around $-0.1T_0$, as shown in Fig. 3(c). Figure 3(b) further shows the differences of the generated IAPs at different radial positions ($r = 0$, 2.5, and 5 μm) driven by the asymmetric pulses, the attosecond pulse durations at these radial positions are 133 as ($r = 0$ μm, red line), 106 as ($r = 2.5$ μm, blue line), and 104 as ($r = 5$ μm, black line), respectively. However, compared with the asymmetric case, the harmonics generated by the symmetric pulse exhibit APTs in the entire 10-μm region. As will be seen below, the above different features of the generated harmonic spectrum and the corresponding attosecond pulses between the two laser pulses are the result of the different phase-matching conditions during the macroscopic propagation.

B. Phase-matching analysis of the harmonic emissions

In order to clarify the physical mechanism of the generated IAP after macroscopic propagation we next analyze the phase-matching conditions of the smooth continuous broad-
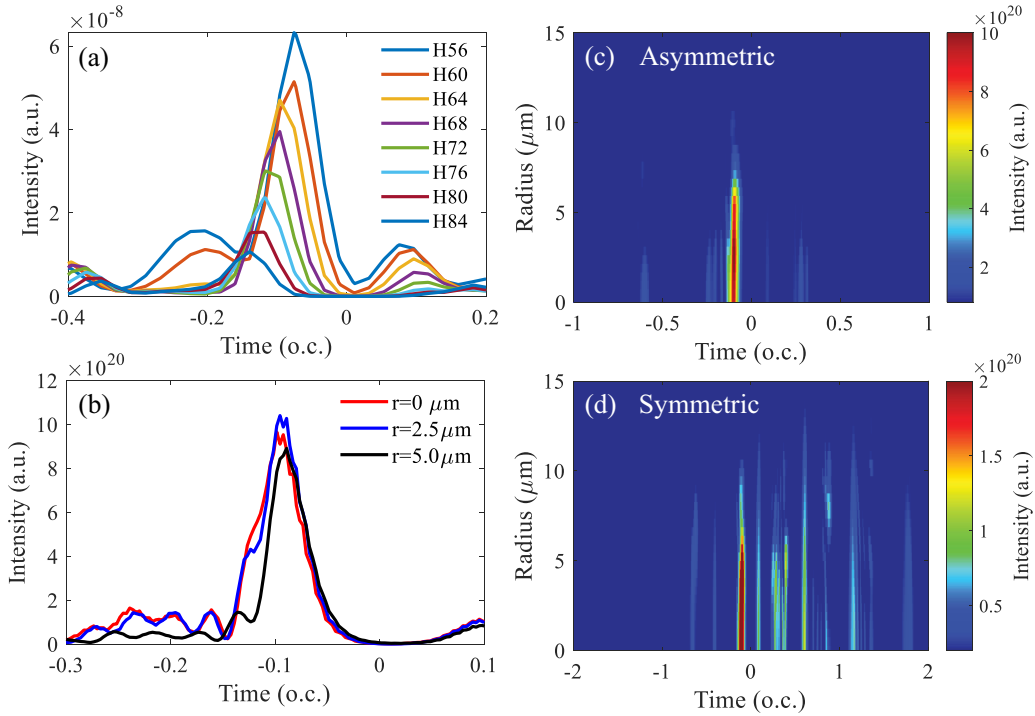
FIG. 3. (a) The emission intensity of different harmonic orders from H56 to H84 varies with time in the asymmetric laser pulse, which is obtained from the time-frequency analysis in Fig. 2(c) at 900 Torr gas pressure. (b) The generated IAPs at $r = 0$ μm [red (middle) line], 2.5 μm [blue (upper) line], and 5 μm [black (lower) line] driving by the asymmetric pulse. (c), (d) The spatial distribution of the generated attosecond pulses driven by the two kinds of laser pulses; the range of high-order harmonics used for the pulse synthesis is H56–H84.

band harmonics in both kinds of laser pulses. Because the attosecond bursts are nearly the same at different radial positions in both cases, as shown in Figs. 3(c) and 3(d), only the on-axis ($r = 0$ μm) phase-matching conditions are taken into consideration in the following. Firstly, we investigate the time-dependent phase mismatching $|\Delta k|$ of the harmonics above H60 at different positions of the gas medium in the case of the symmetric pulse, as shown in Fig. 4. For a better understanding of the relation of the electron ionization and harmonic emission, we also present the dependence of the classical electron energy on the ionization (red circles) and recombination (blue stars) time by the semiclassical three-step model, as shown in Fig. 4(a). One can see that there are three maximum harmonic emission peaks (recombination times) denoted by P_1, P_2, and P_3 in Fig. 4(a) which are located around $-0.3T_0$, $0.2T_0$, and $-0.8T_0$, respectively, and the corresponding ionization times are denoted by P_1' ($-0.95T_0$), P_2' ($-0.45T_0$), and P_3' ($-1.45T_0$). For the harmonics above H60, the electrons of the three harmonic emission peaks are ionized in the region from $-0.99T_0$ to $-0.89T_0$, $-0.49T_0$ to $-0.39T_0$, and $-1.49T_0$ to $-1.39T_0$, respectively. Figures 4(b)–4(e) present the time-dependent phase mismatching of the long (b,d) and short (c,e) paths at the position near the entrance ($z = 0.1$ mm) and the middle ($z = 0.6$ mm). When the propagation distance $z = 0.1$ mm, the values of $|\Delta k_l|$ (the phase mismatching of the long path) in the time interval from $-2.45T_0$ to $-0.8T_0$ and $-0.6T_0$ to $0T_0$ are much smaller than those at other times, as shown in Fig. 4(b), which indicates that all of the three harmonic emission peaks are phase matches well near the entrance of the gas medium. Therefore, the

harmonics above H60 generated at $z = 0.1$ mm have three attosecond bursts in the time domain and exhibit APTs, which is in agreement with the results of the time-frequency analysis in Fig. 4(f). However, because of the macroscopic effect during the propagation, the phase matching becomes more difficult, and only the values of $|\Delta k_l|$ in the time interval from $-1.5T_0$ to $-0.8T_0$ and $-0.2T_0$ to $-0.1T_0$ are much smaller than those in other times at $z = 0.6$ mm, as shown in Fig. 4(d), which indicates that the harmonic emission from peak P_1 is better phase matched than that from peak P_2 and peak P_3. Therefore, the harmonic emissions from peak P_1 are stronger than those from peaks P_2 and P_3, which is in agreement with the time-frequency analysis results in Fig. 4(g). On the other hand, it is clear that compared with the phase mismatching of the long path ($|\Delta k_l|$), the phase mismatching of the short path ($|\Delta k_s|$) at different propagation distances is much greater. This means that the long-path branch is much stronger than the short-path one in the attosecond bursts at different propagation positions. In particular, the attosecond burst at $z = 0.6$ mm has only the long-path emission branch, which results in IAP generation. Therefore, we can conclude that, in the case of the asymmetric laser pulse, good phase-matching conditions of the harmonic emission originating from the long electron trajectories in peak P_1 are obtained during the macroscopic propagation at 900 Torr, which results in continuous broadband harmonic (from H56 to H84) generation and exhibits an IAP with a short pulse duration.

Figure 5 shows the ionization and recombination time obtained from the semiclassical three-step model and phase-matching conditions of the HHG driven by the symmetric
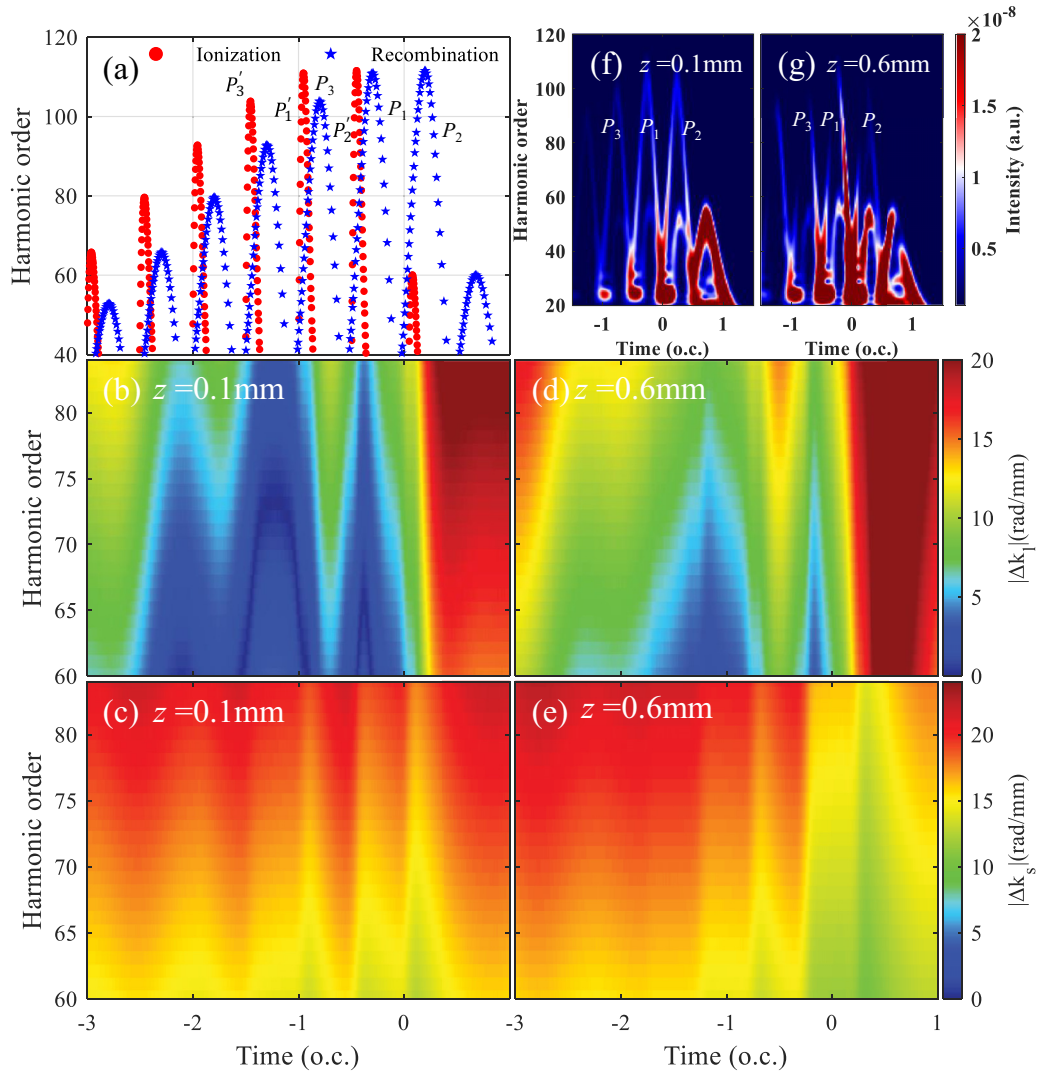
FIG. 4. (a) Harmonic order as a function of the ionization time (red circles) and recombination time (blue stars) obtained from the semiclassical three-step model based on the single-atom response in the case of the asymmetric laser pulse. (b)–(e) On-axis time-dependent phase mismatching of long (b), (d) and short (c), (e) paths as a function of harmonic order at the propagation distances of $z = 0.1$ mm (b), (c) and $z = 0.6$ mm (d), (e) in the case of the asymmetric laser pulse at 900 Torr gas pressure. (f), (g) Time-frequency analysis of the HHG driven by the asymmetric laser pulse with the gas pressure of 900 Torr at the position of $z = 0.1$ mm and $z = 0.6$ mm.

laser pulses at $z = 0.1$ mm and $z = 0.6$ mm, and the corresponding time-frequency analysis results. One can see that, compared with the asymmetric pulse, the phase matching originating from the long electron trajectories is good in the time interval from $-2.0T_0$ to $0T_0$ at the two propagation positions, as shown in Figs. 5(b) and 5(d). It is indicated that the harmonic intensities above H40 from the three maximum harmonic emission peaks are much stronger than the harmonics of other emission peaks during the propagation, which leads to APT generation, as shown in Figs. 5(f) and 5(g). Nevertheless, with the increase of the propagation distance, the values of $|\Delta k_l|$ above H60 become great, which indicates that the harmonic intensities above H60 become weak at $z = 0.6$ mm due to the phase mismatching, which is in agreement with the result in Fig. 5(g). Besides, by comparing the results in Figs. 5(d) and 4(d), it is clear that the phase mismatching of the long path above H60 in the case of the symmetric pulse is much greater than that in the case of the asymmetric pulse,

so the obtained attosecond pulse intensity by superimposing high-order harmonics from H56 to H84 in the symmetric pulse is much weaker than that in the asymmetric case, as shown in Fig. 2(b). It is worth noting that for both kinds of laser pulses, the phase mismatching of the long path ($|\Delta k_l|$) is smaller than that of the short path ($|\Delta k_s|$). However, the phase mismatching $|\Delta k_s|$ of the short path in the case of the symmetric pulse is much smaller than that in the case of the asymmetric pulse. This means that for each attosecond burst, the long-trajectory branch is much stronger than the short-trajectory one in the case of the asymmetric pulse, but the intensities of the two branches are comparable for the symmetric pulse, which is in agreement with the results in Fig. 2.

Because the output harmonic spectrum at the exit of the gas medium is a macroscopic result of the HHG during the propagation, it is contributed by the superposition of the harmonics generated in each propagation position. Therefore, in order to obtain an IAP with a short pulse duration, good tran-
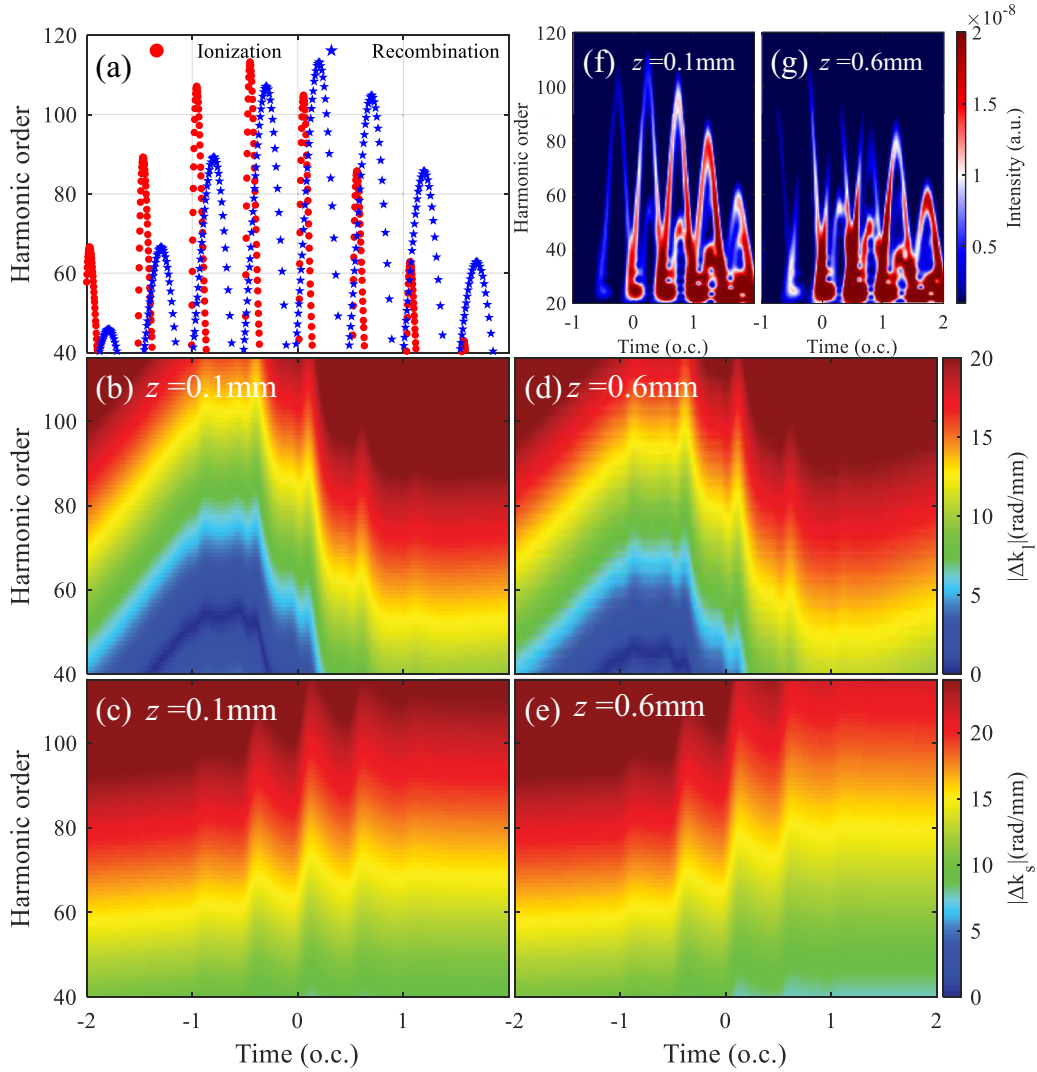
FIG. 5. Same as Fig. 4 except with a symmetric driving laser pulse.

sient phase matching along the propagation should be fulfilled [66]. For 900 Torr gas pressure, we have also investigated the spatiotemporal phase-matching maps along the propagation axis driven by the asymmetric and symmetric laser pulses, respectively, and the results are shown in Figs. 6(a)–6(d), which display the phase mismatching of the long path and short path at H70. It can be seen that in the case of the asymmetric pulse, the long-path phase mismatching $|\Delta k_l|$ of H70 nearly always keeps relatively small values in the time interval from $-1.25T_0$ to $-0.85T_0$ for a long propagation distance ($\sim$0.8 mm), as shown in Fig. 6(a). This means that in the asymmetric pulse, the harmonic emission from peak P_1 in Fig. 4 is better phase matched than that from other peaks during the long-distance propagation, which leads to continuous broadband harmonic generation and contributes to IAP generation. However, in the case of the symmetric pulse, although there is also a phase-matched time window from $-1.2T_0$ to $-0.2T_0$ that exists for a long propagation distance ($\sim$0.9 mm), as shown in Fig. 6(b), this phase-matched time window is too wide to generate the continuous harmonic spectrum. In addition, it can also be seen that in both kinds of laser pulses, the phase mismatching of the short path is always greater than that

of the long path during the propagation, as shown in Figs. 6(c) and 6(d), which indicates that the harmonic emission from the long electron trajectories is enhanced but that from the short electron trajectories is suppressed in the whole macroscopic propagation at 900 Torr gas pressure.

Figures 6(e) and 6(f) show the time-dependent phase mismatching of the long path of H70 at $z = 0.3$ mm and $z = 0.6$ mm in the case of asymmetric (solid line) and symmetric (dashed line) laser pulses. It can be seen that the difference in the phase mismatching of the harmonics driven by both kinds of laser pulses is mainly attributed to the intrinsic harmonic dipole phase mismatching Δk_{dl} (blue line). The values of Δk_{dl} in the pulse leading edge in the case of the asymmetric laser are much smaller than that in the symmetric laser, which leads to better phase-matched harmonics generated in the asymmetric laser pulse. Moreover, compared with the case of the symmetric pulse where the Δk_{dl} changes slowly with time, Δk_{dl} in the case of the asymmetric pulse exhibits some fluctuations, as shown by the shadow in Figs. 6(e) and 6(f), which contributes to obtaining transient phase matching and IAP generation. Because the intrinsic harmonic dipole phase mismatching is laser intensity dependent, these fluctuations
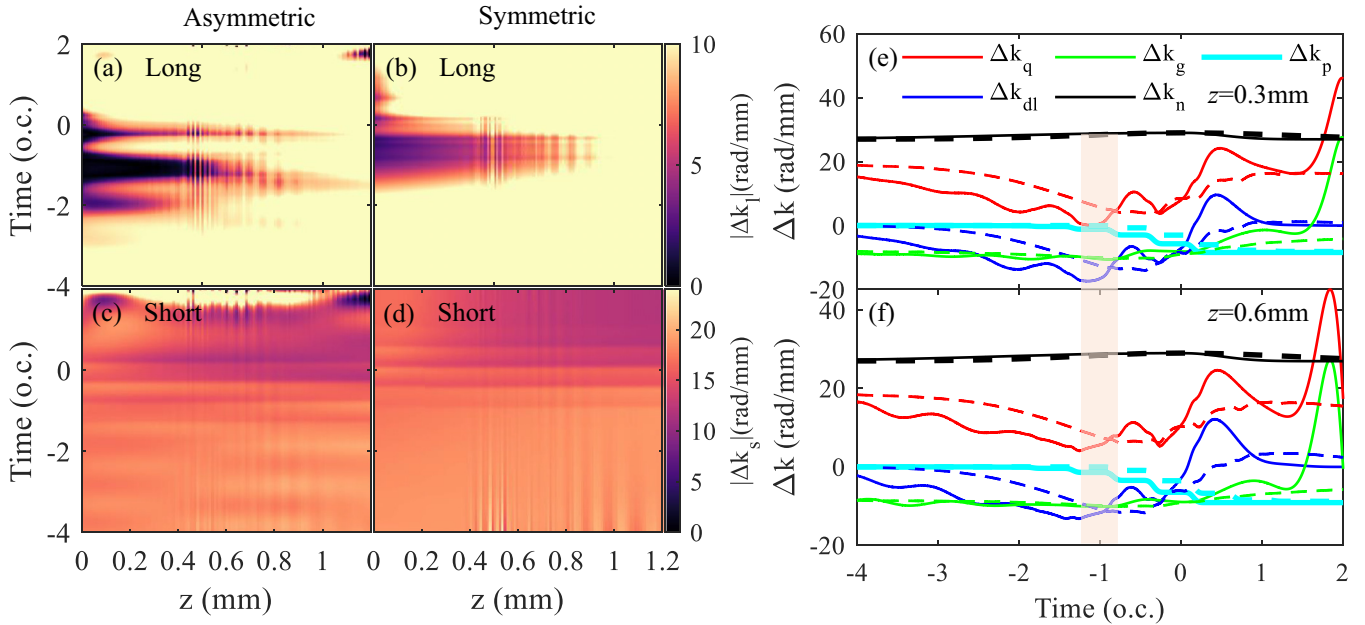
FIG. 6. (a–d) Spatiotemporal phase-matching maps of H70 along the propagation axis driven by the asymmetric (a), (c) and symmetric laser pulses (b), (d); the gas pressure is 900 Torr. (a), (b) denote the long-path phase matching, and (c), (d) denote the short-path phase matching. (e), (f) The time-dependent phase mismatching of H70 from the long-electron trajectory emissions at $z = 0.3$ mm (e) and $z = 0.6$ mm (f) in the case of asymmetric (solid line) and symmetric (dashed line) laser pulses; the gas pressure is 900 Torr. The black (upper dark gray) line, red (middle dark gray) line, blue (lower dark gray line), cyan (thick light gray), and green (thin light gray) line in (e), (f) denote the phase-mismatching values of Δk_n, Δk_q, Δk_{dl}, Δk_p, and Δk_g, respectively.

of Δk_{dl} in the time domain can be attributed to the spatiotemporal reshaping of the temporal asymmetric laser waveform when propagating in the gas medium at high pressure. This spatiotemporal reshaping of the driving laser during the propagation is caused by the nonlinear propagation effects, such as spatial diffraction, nonlinear self-focusing, ionization, plasma defocusing, and so on [67–69] (see Appendix A). It is worth noting that the shadow with a large fluctuation of Δk_{dl} in Figs. 6(e) and 6(f) locates around $-1.0T_0$, which is just within the ionization time window of the harmonic emission peak P_1 in Fig. 4 that leads to IAP generation with short pulse duration at the exit of the gas medium. Furthermore, the investigation of the spatial long-path phase mismatching $|\Delta k_{dl}|$ also showed that there is a significant difference in the phase mismatching of H70 in space (z, r) at different times in the case of the asymmetric laser pulse, which also resulted in IAP generation. However, the spatial phase mismatching is nearly the same at different times in the case of the symmetric laser pulse, which is unable to support IAP generation, as shown in Appendix B.

C. Effects of gas pressure on harmonic emissions

It has been mentioned that measured high-order harmonics are the macroscopic response to the gas medium, and many studies have shown that the HHG spectrum and the synthesized attosecond pulse are changed with the gas pressure of the medium [70–73]. Therefore, in this work, we have also investigated the effect of gas pressure on the HHG spectrum and attosecond pulses in both kinds of laser pulses. Figure 7 shows the time-frequency analysis results of the harmonic spectra driven by the asymmetric (a–c) and symmetric (d–f)

laser pulses at gas pressures of 600, 700, and 800 Torr, respectively. We can see that in the case of the asymmetric laser pulse, the attosecond burst in each o.c. at 600 Torr has only one major emission branch with positive chirp which results from the short-electron trajectories, as shown in Fig. 7(a). However, when the gas pressure increases to 700 Torr, as shown in Fig. 7(b), each attosecond burst has two emission branches, which means that both long- and short-electron trajectories simultaneously contribute to harmonic emission. As the gas pressure increases to 800 Torr, there is only the long-electron-trajectory emission branch with negative chirp existing in each attosecond burst, as shown in Fig. 7(c). According to the analyzed results above, we know that the different features of the attosecond burst at different gas pressures are caused by the different phase-matching conditions of the HHG in the macroscopic gas medium [73]. In particular, at 800 Torr, there is only one strong attosecond burst above H57 existing between $-2.0T_0$ and $2.0T_0$, which locates around $-0.1T_0$. This means that the harmonic emissions above H57 driven by the asymmetric laser pulse at 800 Torr have continuous spectra with broadband and support IAP generation with a short duration, which is similar to the result at 900 Torr. However, in the case of the symmetric laser pulse, although the long-electron-trajectory emission branch in each attosecond burst at 800 Torr is stronger than the short-electron-trajectory one, as shown in Fig. 7(f), each of the attosecond bursts at 600 and 700 Torr has two emission branches with nearly identical intensity, as shown in Figs. 7(d) and 7(e). In addition, the time-frequency analysis results show that, compared with the case of the asymmetric pulse, the harmonics generated by the symmetric laser pulse are always unable to form continuous spectra at different gas pressures.
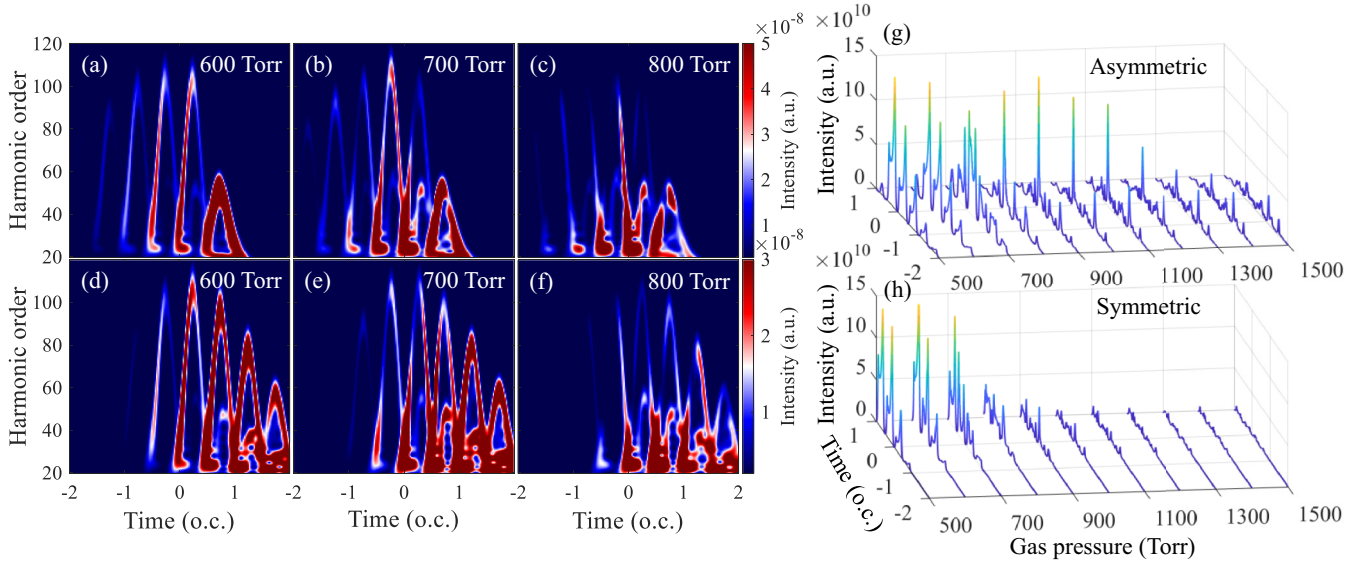
FIG. 7. (a)–(f) Time-frequency analysis of near-field HHG at the exit plane of the gas medium driven by the asymmetric (a)–(c) and symmetric (d)–(f) laser pulses at different gas pressures. The laser and gas medium parameters used here are the same as that in Fig. 1 except for the gas pressure. (g), (h) Attosecond pulses which are obtained by superimposing selected high-order harmonics at different gas pressures generated by the asymmetric (g) and symmetric (h) laser pulses. The range of high-order harmonics used for the attosecond pulse synthesis at different gas pressures is presented in the text.

More intuitively, we have also investigated the synthesized attosecond pulses by superimposing selected high-order harmonics driven by both kinds of laser pulses at different gas pressures, and the results are shown in Fig. 7(g) (asymmetric pulse) and Fig. 7(h) (symmetric pulse). The range of high-order harmonics used for the attosecond pulse synthesis in both kinds of laser pulses are H60–H110 for 500–700 Torr, H57–H100 for 800 Torr, H56–H84 for 900 Torr, H53–H71 for 1000 Torr, H45–H62 for 1100–1200 Torr, and H37–H52 for 1300–1500 Torr, respectively. It is clear that in the case of the asymmetric laser pulse, as shown in Fig. 7(g), when gas pressure is below 700 Torr, the harmonic emissions exhibit APTs in the time domain and the intensity decreases with the increase of the gas pressure. However, when the gas pressure is in the range of 800–1200 Torr, we can see that the harmonic emissions exhibit an IAP in the time domain with a pulse duration of 154 as (800 Torr), 117 as (900 Torr), 122 as (1000 Torr), 136 as (1100 Torr), and 160 as (1200 Torr), respectively. When the gas pressure is above 1200 Torr, the intensity of the harmonic emission decreases rapidly and is unable to form the IAP. The results above can be attributed to the phase-matching conditions of the harmonics during the macroscopic propagation at different gas pressure. When the gas pressure is low (<800 Torr), the spatiotemporal reshaping of the laser pulse is too weak to result in the fluctuations of the intrinsic harmonic dipole phase mismatching, so a wide phase-matched time window is formed, which leads to the APT generation. As the gas pressure increases to 800 Torr, a suitable spatiotemporal reshaping of the laser pulse leads to the fluctuations of the intrinsic harmonic dipole phase mismatching and a transient phase matching is obtained for the IAP generation. We can see in Fig. 7(g) the gas pressure range that forms the transient phase matching is 800–1200 Torr, in which the optimal gas pressure is 900 Torr. When the gas

pressure increases further (>1200 Torr), the phase matching becomes more difficult for the high pressure so that the intensity and cutoff energy of the generated harmonics dropped rapidly. Similar to the case of the asymmetric pulse, the harmonic emissions at low gas pressure (<700 Torr) in the case of the symmetric pulse also exhibit APTs due to the wide phase-matched time window, as shown in Fig. 7(h). But different from the case of the asymmetric pulse, the intensity of the harmonic emissions at high gas pressure (>800 Torr) in the case of the symmetric pulse drops rapidly and is unable to form the IAP, which is also due to the difficulty of the phase matching at high gas pressures. Therefore, we can conclude that the broadband of the continuous high-order harmonic spectra and the pulse width of the synthesized attosecond pulses can be controlled by changing the gas pressure in the case of the asymmetric laser pulse.

D. Chirp effects in laser pulse on the harmonic emissions

We have demonstrated that macroscopic IAPs can be generated by using a chirped-free temporal asymmetric laser pulse. However, the temporally asymmetric laser pulse formed through the self-steepening effect in a transparent medium usually exhibits dispersion and chirping in the frequency domain, which could affect the harmonic emission process [74,75]. Therefore, it is necessary to study the chirp effects of the asymmetric laser pulse on harmonic emission. The laser field with chirp can be expressed as

$$E(t) = E_0 f(t)\cos(\omega t + \alpha t^2), \tag{23}$$

where the time envelope function $f(t)$ in asymmetric and symmetric laser pulses is given by Eq. (10) and α is the linear chirp rate. It is convenient to introduce a dimensionless chirp parameter which is defined by $\beta = \alpha \tau_0^2 / 2\ln 2$, where $\tau_0 = 3T_0$
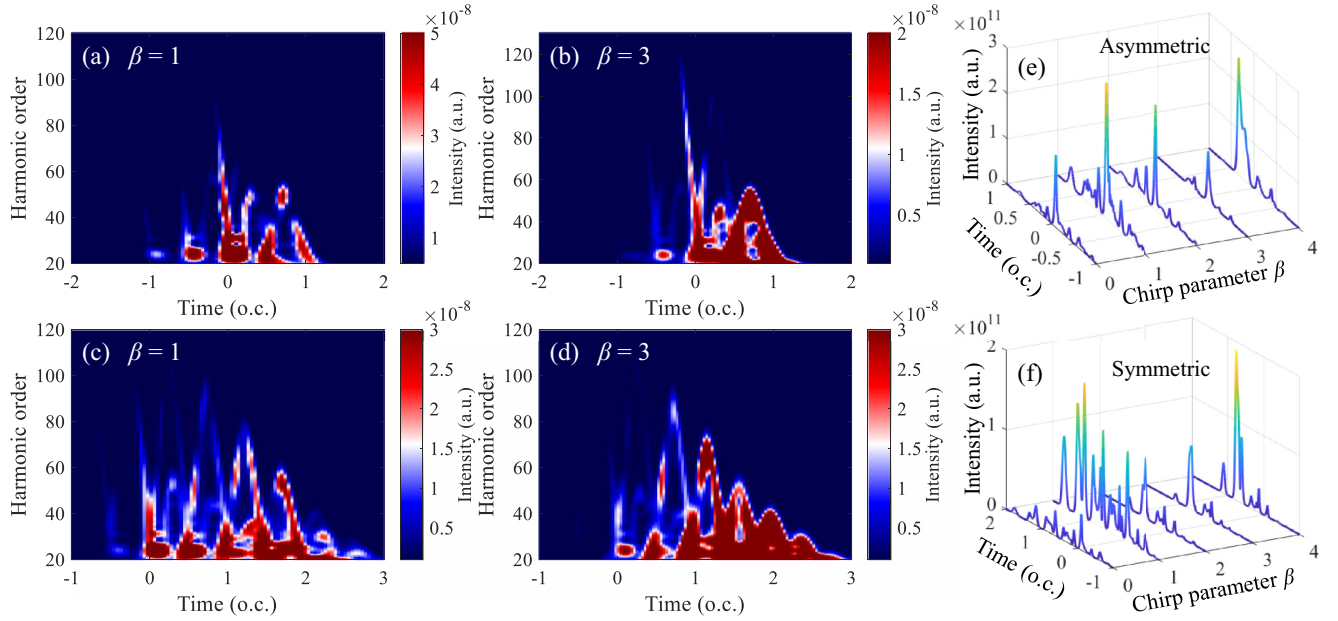
FIG. 8. (a)–(d) Time-frequency analysis of near-field HHG at the exit plane of the gas medium driven by the asymmetric (a), (b) and symmetric (c), (d) laser pulses with different chirp parameters at 900 Torr gas pressure. (e), (f) Attosecond pulses which are obtained by superimposing selected high-order harmonics at different chirp parameters generated by the asymmetric (e) and symmetric (f) laser pulses. The range of high-order harmonics used for the attosecond pulse synthesis at different chirp parameters is presented in the text.

is the pulse width of both kinds of laser pulses. Figure 8 shows the time-frequency analysis results of the harmonic spectra driven by the asymmetric (a,b) and symmetric (c,d) laser pulses with $\beta = 1$ and 3 at 900 Torr gas pressure, respectively. It can be seen that in the case of the asymmetric laser pulse, the harmonic emissions above H56 under these two chirp parameters only exhibit one strong attosecond burst around $-0.1T_0$, which is consistent with the results of the chirped-free pulse and can be attributed to the transient phase matching. This means that the harmonic emissions driven by the asymmetric laser pulse under these two chirp parameters also have continuous spectra with broadband and support the short IAP generation. Moreover, as the chirp parameter increases, the cutoff energy of the high-order harmonics and the bandwidth of the continuum spectrum also increase, as shown in Fig. 8(b), which is beneficial to obtaining a shorter Fourier transform limited attosecond pulse. However, compared with the asymmetric pulse, the harmonics generated by the symmetric laser with $\beta = 1$ are unable to form continuous spectra, as shown in Fig. 8(c), which is also consistent with the results of the chirped-free pulse. However, when the chirp parameter is increased to $\beta = 3$, as shown in Fig. 8(d), the harmonic generation due to the changes in the driving laser waveform exhibits a narrowband continuum above H77, which appears as a broad IAP in the time domain.

In order to demonstrate more clearly the chirp effects in laser pulses on IAP generation, we also investigated the synthesized attosecond pulses by superimposing selected high-order harmonics under different chirp parameters, as shown in Fig. 8(e) (asymmetric pulse) and Fig. 8(f) (symmetric pulse). The range of high-order harmonics used for the attosecond pulse synthesis in asymmetric laser pulses is H56–H84 for $\beta = 0$ to $\beta = 2$, H57–H122 for $\beta = 3$, and H57–H100 for $\beta = 4$, respectively, as shown in Fig. 8(e). It

can be seen that the harmonic emissions under chirp parameters of $\beta = 0$ to $\beta = 4$ always exhibit IAP in the time domain and the pulse duration is 117 as ($\beta = 0$), 141 as ($\beta = 1$), 120 as ($\beta = 2$), 136 as ($\beta = 3$), and 254 as ($\beta = 4$), respectively. For the case of the symmetric laser pulse, the range of superimposed high-order harmonics for the attosecond pulse synthesis is H56–H84 for $\beta = 0$ to $\beta = 2$, H77–H94 for $\beta = 3$, and H70–H94 for $\beta = 4$, respectively, as shown in Fig. 8(f). We can see that the IAP is exhibited in high-order harmonic emissions generated by the symmetric pulse only when the chirp parameter is comparatively large, such as $\beta = 3$ and 4. The corresponding pulse duration of the synthesized IAP for $\beta = 3$ and $\beta = 4$ is 300 and 275 as, respectively. Therefore, by comparing the results of both kinds of laser pulses with different chirp parameters, we can confirm that by using the asymmetric laser pulse with different chirp parameters, macroscopic IAPs with a similar pulse duration can also be produced.

IV. CONCLUSION

In conclusion, we theoretically investigated the phase-matching mechanisms of macroscopic harmonic spectra and isolated attosecond pulses generated by a temporal asymmetric laser pulse with 800-nm wavelength. Firstly, we compared the near-field high-order harmonics spectra at the exit plane of the gas medium at 900 Torr gas pressure driven by the asymmetric and symmetric laser pulses, respectively. We found that the generated harmonic spectra in the region from H56 to H84 driven by the asymmetric pulse exhibit a smooth continuous broadband (43 eV) spectrum structure. By superimposing selected high-order harmonics (H56–H84) an IAP with a pulse duration of 117 as was obtained, which locates around $-0.1T_0$. For a better understanding of the emission features

of the harmonics in the case of the asymmetric laser pulse, we also analyzed the time-frequency pictures of the harmonic emissions at the exit of the gas medium. The results showed that the harmonics above H60 have only one attosecond burst in the time domain which mainly originated from the long-electron-trajectory emission branch and contributed most to the IAP generation. However, compared with the asymmetric pulse, the harmonics generated by the symmetric laser were unable to form a smooth continuous spectrum structure where the synthesized attosecond pulses exhibited APTs in the time domain. Secondly, in order to clarify the physical mechanism of the generated IAP after macroscopic propagation, we also analyzed the phase-matching conditions of the HHG in both kinds of laser pulses. We found that the harmonic emissions from the long-trajectory electrons in the case of the asymmetric pulse were better phase matched than that of the short-trajectory electrons and the harmonic emissions in the case of the symmetric laser pulse. Furthermore, we also investigated the spatiotemporal phase-matching maps of H70 in both kinds of laser pulses at 900 Torr gas pressure. The results showed that the harmonic emissions from the long-trajectory electrons in the case of the asymmetric pulse exhibited a good transient phase matching for a long distance during the macroscopic propagation, which led to continuous broadband harmonic generation and contributed to IAP generation. By analyzing the four components of the time-dependent phase mismatching of the long-trajectory electron emissions, we found that compared with the phase mismatching of the harmonics in the symmetric pulse, the intrinsic harmonic dipole phase mismatching of the long-trajectory electron emissions

in the case of the asymmetric pulse exhibited some fluctuations in the time domain in the pulse leading edge during the macroscopic propagation, which resulted in the formation of the transient phase matching. This fluctuation of the phase mismatching could be attributed to the spatiotemporal reshaping of the laser waveform in the case of the asymmetric pulse when propagating in the gas medium with high pressure. Thirdly, we studied the effect of the different gas pressure on macroscopic HHG and IAP and found that the spatiotemporal waveform of the laser field in the case of the asymmetric pulse can be controlled by gas pressure, which in turn forms the different phase-matching conditions appropriate only for short- or long-trajectory electron emissions. In particular, when the gas pressure is in the range from 800 to 1200 Torr, a "suitable" spatiotemporal reshaping of the asymmetric laser pulse could be formed to lead to the fluctuations of the phase mismatching, so that a transient phase matching is obtained and an IAP is generated with short pulse duration in this gas pressure range. Lastly, the chirp effects in both kinds of laser pulses on the harmonic emissions were also investigated. The results showed that macroscopic IAPs can also be produced in the case of a asymmetric laser pulse even if the chirp parameter was changed and the generated IAPs have a similar pulse duration with the results in the chirped-free laser pulse as long as the chirp parameter was not excessively large.

Therefore, by using a temporal asymmetric laser field, a smooth continuous harmonic spectrum structure can be obtained during the macroscopic propagation, which will exhibit an IAP with a short pulse duration in the time domain. It
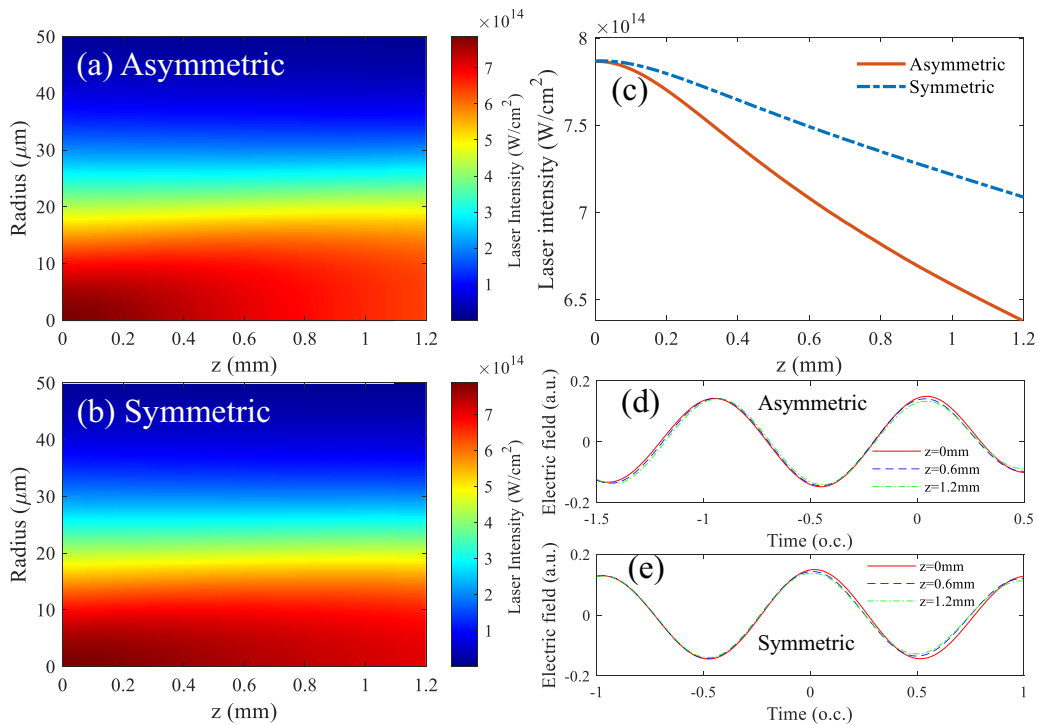

FIG. 9. The spatial evolution of the asymmetric (a) and symmetric (b) laser pulse propagated in the gas medium. (c) on-axis ($r = 0$) laser intensity evolution along the propagation axis in both kinds of laser pulses. (d), (e) The electric field of the asymmetric (d) and symmetric (e) driving laser at the entrance ($z = 0$) (red solid line), middle ($z = 0.6$ mm) [dashed blue (dark gray) line], and exit ($z = 1.2$ mm) [dashed green (light gray) line] of the gas medium. The gas pressure is 900 Torr.
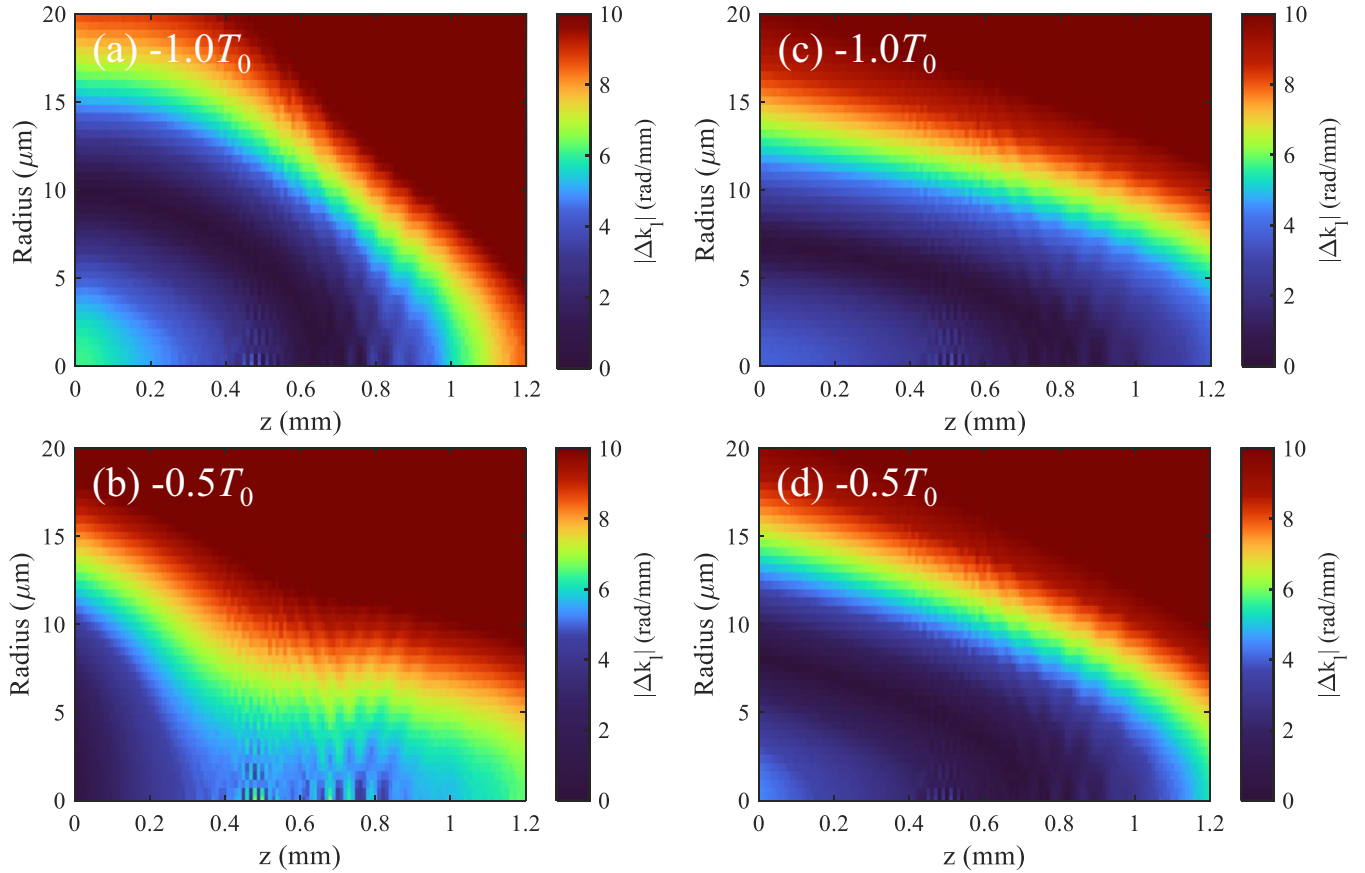
FIG. 10. The spatial long-path phase mismatching of H70 at $-1.0T_0$ and $-0.5T_0$ driven by the asymmetric (a), (b) and symmetric (c), (d) laser pulses, in which the gas pressure is 900 Torr.

is worth noting that HHG is the macroscopic response to the generation medium and is very sensitive to the properties of the driving lasers and the gas medium. In order to generate the IAPs with the shortest pulse duration in experiments, the width of the pulse leading edge and trailing edge in the asymmetric pulse may be different at different gas pressure, gas medium, laser pulse duration, chirp parameters, and so on. Thus, our study provides an efficient approach for the experimental work on the IAP generation in the future.

APPENDIX A: EVOLUTION OF THE LASER FIELD IN THE MEDIUM

When the driving laser propagated in the gas medium with high gas pressure, its intensity decreased rapidly due to the nonlinear propagation effects, such as spatial diffraction, material dispersion, nonlinear self-focusing, ionization, plasma

defocusing, and so on, which led to the spatial reshaping of the driving laser, as shown in Figs. 9(a)–9(c) [67–69]. Because of their different temporal shapes, the spatial evolution is different in both kinds of laser pulses; the spatial reshaping of the asymmetric laser pulse is stronger than that of the symmetric laser pulse. In addition, these nonlinear propagation effects also led to the peak electric field shift in time in both kinds of laser pulses when propagating through the gas medium; this is the temporal reshaping of the driving laser. Furthermore, the time shift of the peak electric field in the asymmetric laser pulse is larger than that in the symmetric laser, especially in the pulse leading edge, as shown in Figs. 9(d) and 9(e). Therefore, it is the difference in the spatiotemporal reshaping of the two kinds of driving laser pulses that resulted in the different phase matching of the harmonics in space and time.

APPENDIX B: SPATIAL PHASE MISMATCHING OF THE HARMONICS

Because the dispersion phase mismatching of the neutral atomic and free electrons is gas pressure and ionization probability dependent, and the gas pressure $P(z)$ and ionization probability $p(z, t)$ is spatial and time dependent, so the phase mismatching due to the neutral atomic dispersion and plasma dispersion are time (t) and space (z, r) dependent. In addition, the intrinsic harmonic dipole phase mismatching and the geometrical phase mismatching are dependent on the intensity

gradient and the phase gradient of the laser, which can be changed with space and time due to the spatiotemporal reshaping during the propagation [76,77], as shown in Fig. 9. Therefore, the total phase mismatching is also time and space dependent and can be calculated in the simulation. Figure 10 shows the spatial (z, r) phase mismatching of the H70 emitted from the long trajectory at $-1.0T_0$ and $-0.5T_0$ in both kinds of laser pulses. It can be seen that the phase mismatching of HHG in the asymmetric laser pulse is different for $-1.0T_0$ and $-0.5T_0$. The phase mismatching of H70 at $-1.0T_0$ nearly keeps relatively small values within the 0–10-μm region in the radial direction for the entire gas medium, as shown in Fig. 10(a), which is just within the ionization time window of

the harmonic emission peak P_1 in Fig. 4. However, the phase mismatching of H70 at $-0.5T_0$ only keeps relatively small values for the first 0.3-mm region, as shown in Fig. 10(b). It is the significant difference of the phase mismatching at different times in the case of the asymmetric laser pulse that resulted in the IAP generation. Compared with the asymmetric laser pulse, the spatial phase mismatching of H70 in the symmetric laser pulse at $-1.0T_0$ and $-0.5T_0$ is nearly the same, and keeps relatively small values within the 0–10-μm region in the radial direction for the entire gas medium, as shown in Figs. 10(c) and 10(d). Therefore, there is no significant difference in the phase mismatching at different times in the case of the symmetric laser pulse, which leads to the APT generation.

[1] A. McPherson, G. Gibson, H. Jara, U. Johann, T. S. Luk, I. A. McIntyre, K. Boyer, and C. K. Rhodes, J. Opt. Soc. Am. B **4**, 595 (1987).

[2] P. B. Corkum, N. H. Burnett, and M. Y. Ivanov, Opt. Lett. **19**, 1870 (1994).

[3] M. Hentschel, R. Kienberger, C. Spielmann, G. A. Reider, N. Milosevic, T. Brabec, P. Corkum, U. Heinzmann, M. Drescher, and F. Krausz, Nature (London) **414**, 509 (2001).

[4] F. Krausz and M. Ivanov, Rev. Mod. Phys. **81**, 163 (2009).

[5] E. Goulielmakis, Z.-H. Loh, A. Wirth, R. Santra, N. Rohringer, V. S. Yakovlev, S. Zherebtsov, T. Pfeifer, A. M. Azzeer, M. F. Kling, S. R. Leone, and F. Krausz, Nature (London) **466**, 739 (2010).

[6] L.-Y. Peng, W.-C. Jiang, J.-W. Geng, W.-H. Xiong, and Q. Gong, Phys. Rep. **575**, 1 (2015).

[7] F. Calegari, G. Sansone, S. Stagira, C. Vozzi, and M. Nisoli, J. Phys. B **49**, 062001 (2016).

[8] F. Krausz, Phys. Scr. **91**, 063011 (2016).

[9] J. Biegert, F. Calegari, N. Dudovich, F. Quéré, and M. Vrakking, J. Phys. B **54**, 070201 (2021).

[10] M. Lewenstein, Science **297**, 1131 (2002).

[11] M. Chini, K. Zhao, and Z. Chang, Nat. Photonics **8**, 178 (2014).

[12] K. Midorikawa, Nat. Photonics **16**, 267 (2022).

[13] P. B. Corkum, Phys. Rev. Lett. **71**, 1994 (1993).

[14] G. Sansone, E. Benedetti, F. Calegari, C. Vozzi, L. Avaldi, R. Flammini, L. Poletto, P. Villoresi, C. Altucci, R. Velotta, S. Stagira, S. De Silvestri, and M. Nisoli, Science **314**, 443 (2006).

[15] I. J. Sola, E. Mével, L. Elouga, E. Constant, V. Strelkov, L. Poletto, P. Villoresi, E. Benedetti, J. P. Caumes, S. Stagira, C. Vozzi, G. Sansone, and M. Nisoli, Nat. Phys. **2**, 319 (2006).

[16] J. Li, X. Ren, Y. Yin, K. Zhao, A. Chew, Y. Cheng, E. Cunningham, Y. Wang, S. Hu, Y. Wu, M. Chini, and Z. Chang, Nat. Commun. **8**, 186 (2017).

[17] E. Goulielmakis, M. Schultze, M. Hofstetter, V. S. Yakovlev, J. Gagnon, M. Uiberacker, A. L. Aquila, E. M. Gullikson, D. T. Attwood, R. Kienberger, F. Krausz, and U. Kleineberg, Science **320**, 1614 (2008).

[18] Z. Minjie, Y. Peng, T. Hao, H. Xinkui, Z. Wei, Z. Shiyang, W. Lifeng, Y. Chenxia, and W. Zhiyi, Chin. Phys. Lett. **30**, 093201 (2013).

[19] T. Gaumnitz, A. Jain, Y. Pertot, M. Huppert, I. Jordan, F. Ardana-Lamas, and H. J. Wörner, Opt. Express **25**, 27506 (2017).

[20] H. Mashiko, S. Gilbertson, C. Li, S. D. Khan, M. M. Shakya, E. Moon, and Z. Chang, Phys. Rev. Lett. **100**, 103906 (2008).

[21] X. Feng, S. Gilbertson, H. Mashiko, H. Wang, S. D. Khan, M. Chini, Y. Wu, K. Zhao, and Z. Chang, Phys. Rev. Lett. **103**, 183901 (2009).

[22] K. Zhao, Q. Zhang, M. Chini, Y. Wu, X. Wang, and Z. Chang, Opt. Lett. **37**, 3891 (2012).

[23] X. Wang, L. Wang, F. Xiao, D. Zhang, Z. Lü, J. Yuan, and Z. Zhao, Chin. Phys. Lett. **37**, 023201 (2020).

[24] E. J. Takahashi, P. Lan, O. D. Mücke, Y. Nabekawa, and K. Midorikawa, Phys. Rev. Lett. **104**, 233901 (2010).

[25] E. J. Takahashi, P. Lan, O. D. Mücke, Y. Nabekawa, and K. Midorikawa, Nat. Commun. **4**, 2691 (2013).

[26] B. Li, X. Tang, K. Wang, C. Zhang, Z. Guan, B. Wang, C. D. Lin, and C. Jin, Phys. Rev. Applied **18**, 034048 (2022).

[27] T. Pfeifer, L. Gallmann, M. J. Abel, D. M. Neumark, and S. R. Leone, Opt. Lett. **31**, 975 (2006).

[28] B. Xue, Y. Tamaru, Y. Fu, H. Yuan, P. Lan, O. D. Mücke, A. Suda, K. Midorikawa, and E. J. Takahashi, Sci. Adv. **6**, eaay2802 (2020).

[29] B. Xue, Y. Tamaru, Y. Fu, H. Yuan, P. Lan, O. D. Mücke, A. Suda, K. Midorikawa, and E. J. Takahashi, Ultrafast Sci. **2021**, 9828026 (2021).

[30] T. Pfeifer, A. Jullien, M. J. Abel, P. M. Nagel, L. Gallmann, D. M. Neumark, and S. R. Leone, Opt. Express **15**, 17120 (2007).

[31] M. J. Abel, T. Pfeifer, P. M. Nagel, W. Boutu, M. J. Bell, C. P. Steiner, D. M. Neumark, and S. R. Leone, Chem. Phys. **366**, 9 (2009).

[32] F. Ferrari, F. Calegari, M. Lucchini, C. Vozzi, S. Stagira, G. Sansone, and M. Nisoli, Nat. Photonics **4**, 875 (2010).

[33] H. Vincenti and F. Quéré, Phys. Rev. Lett. **108**, 113904 (2012).

[34] K. T. Kim, C. Zhang, T. Ruchon, J.-F. Hergott, T. Auguste, D. M. Villeneuve, P. B. Corkum, and F. Quéré, Nat. Photonics **7**, 651 (2013).

[35] T. J. Hammond, G. G. Brown, K. T. Kim, D. M. Villeneuve, and P. B. Corkum, Nat. Photonics **10**, 171 (2016).

[36] M.-C. Chen, C. Mancuso, C. Hernández-García, F. Dollar, B. Galloway, D. Popmintchev, P.-C. Huang, B. Walker, L. Plaja, A. A. Jaroń-Becker, A. Becker, M. M. Murnane, H. C. Kapteyn, and T. Popmintchev, Proc. Natl. Acad. Sci. USA **111**, E2361 (2014).

[37] J. Schötz, B. Förg, W. Schweinberger, I. Liontos, H. A. Masood, A. M. Kamal, C. Jakubeit, N. G. Kling, T. Paasch-Colberg,

S. Biswas, M. Högner, I. Pupeza, M. Alharbi, A. M. Azzeer, and M. F. Kling, Phys. Rev. X **10**, 041011 (2020).

[38] B. Li, K. Wang, X. Tang, Y. Chen, C. D. Lin, and C. Jin, New J. Phys. **23**, 073051 (2021).

[39] C. Hernández-García, T. Popmintchev, M. M. Murnane, H. C. Kapteyn, L. Plaja, A. Becker, and A. Jaron-Becker, Opt. Express **25**, 11855 (2017).

[40] X. Tang, K. Wang, B. Li, Y. Chen, C. D. Lin, and C. Jin, Opt. Lett. **46**, 5137 (2021).

[41] J. X. Tull, M. A. Dugan, and W. S. Warren, Adv. Magn. Opt. Res. **20**, 1 (1997).

[42] A. M. Weiner, Opt. Commun. **284**, 3669 (2011).

[43] L. Chen, W. Zhu, P. Huo, J. Song, H. J. Lezec, T. Xu, and A. Agrawal, Sci. Adv. **8**, eabq8314 (2022).

[44] J. J. Carrera and S.-I. Chu, Phys. Rev. A **75**, 033807 (2007).

[45] J.-X. Han, J. Wang, Y. Qiao, A.-H. Liu, F.-M. Guo, and Y.-J. Yang, Opt. Express **27**, 8768 (2019).

[46] Y. Xiang, J. Miao, Y. Niu, S. Gong, R. Li, and Z. Xu, J. Phys. B **45**, 115601 (2012).

[47] J. A. Pérez-Hernández, M. F. Ciappina, M. Lewenstein, L. Roso, and A. Zaïr, Phys. Rev. Lett. **110**, 053001 (2013).

[48] J. Luo, Y. Li, Z. Wang, Q. Zhang, and P. Lu, J. Phys. B **46**, 145602 (2013).

[49] J. Wu, Z. Zhai, and X.-S. Liu, Chin. Phys. B **19**, 093201 (2010).

[50] J. Wang, G. Chen, S.-Y. Li, D.-J. Ding, J.-G. Chen, F.-M. Guo, and Y.-J. Yang, Phys. Rev. A **92**, 033848 (2015).

[51] S. Kim, J. Jin, Y.-J. Kim, I.-Y. Park, Y. Kim, and S.-W. Kim, Nature (London) **453**, 757 (2008).

[52] L. Bergé, S. Skupin, R. Nuter, J. Kasparian, and J. P. Wolf, Rep. Prog. Phys. **70**, 1633 (2007).

[53] A. Couairon and A. Mysyrowicz, Phys. Rep. **441**, 47 (2007).

[54] S. L. Stebbings, F. Süßmann, Y. Y. Yang, A. Scrinzi, M. Durach, A. Rusina, M. I. Stockman, and M. F. Kling, New J. Phys. **13**, 073010 (2011).

[55] M. Lewenstein, P. Balcou, M. Y. Ivanov, A. L'Huillier, and P. B. Corkum, Phys. Rev. A **49**, 2117 (1994).

[56] M. Geissler, G. Tempea, A. Scrinzi, M. Schnürer, F. Krausz, and T. Brabec, Phys. Rev. Lett. **83**, 2930 (1999).

[57] E. Priori, G. Cerullo, M. Nisoli, S. Stagira, S. De Silvestri, P. Villoresi, L. Poletto, P. Ceccherini, C. Altucci, R. Bruzzese, and C. de Lisio, Phys. Rev. A **61**, 063801 (2000).

[58] C. Jin, A.-T. Le, and C. D. Lin, Phys. Rev. A **83**, 023411 (2011).

[59] M. V. Ammosov, N. B. Delone, and V. P. Krainov, Sov. Phys. JETP **64**, 1191 (1986).

[60] B. L. Henke, E. M. Gullikson, and J. C. Davis, At. Data Nucl. Data Tables **54**, 181 (1993).

[61] C. Jin, A.-T. Le, and C. D. Lin, Phys. Rev. A **79**, 053413 (2009).

[62] C. Jin, A.-T. Le, C. A. Trallero-Herrero, and C. D. Lin, Phys. Rev. A **84**, 043411 (2011).

[63] X.-M. Tong and S.-I. Chu, Phys. Rev. A **61**, 021802 (2000).

[64] P. Balcou, P. Salières, A. L'Huillier, and M. Lewenstein, Phys. Rev. A **55**, 3204 (1997).

[65] M. B. Gaarde, J. L. Tate, and K. J. Schafer, J. Phys. B **41**, 132001 (2008).

[66] S. M. Teichmann, F. Silva, S. L. Cousin, M. Hemmer, and J. Biegert, Nat. Commun. **7**, 11493 (2016).

[67] C. M. Heyl, H. Coudert-Alteirac, M. Miranda, M. Louisy, K. Kovacs, V. Tosa, E. Balogh, K. Varjú, A. L'Huillier, A. Couairon, and C. L. Arnold, Optica **3**, 75 (2016).

[68] B. Major, O. Ghafur, K. Kovács, K. Varjú, V. Tosa, M. J. J. Vrakking, and B. Schütte, Optica **8**, 960 (2021).

[69] B. Major, K. Kovács, E. Svirplys, M. Anus, O. Ghafur, K. Varjú, M. J. J. Vrakking, V. Tosa, and B. Schütte, Phys. Rev. A **107**, 023514 (2023).

[70] E. Constant, D. Garzella, P. Breger, E. Mével, C. Dorrer, C. Le Blanc, F. Salin, and P. Agostini, Phys. Rev. Lett. **82**, 1668 (1999).

[71] P. Lan, M. Ruhmann, L. He, C. Zhai, F. Wang, X. Zhu, Q. Zhang, Y. Zhou, M. Li, M. Lein, and P. Lu, Phys. Rev. Lett. **119**, 033201 (2017).

[72] Y. Niu, F. Liu, Y. Liu, H. Liang, Y. Yang, R. Ma, and D. Ding, Opt. Commun. **397**, 118 (2017).

[73] Y. Pan, F. Guo, C. Jin, Y. Yang, and D. Ding, Phys. Rev. A **99**, 033411 (2019).

[74] V. Tosa, H. T. Kim, I. J. Kim, and C. H. Nam, Phys. Rev. A **71**, 063808 (2005).

[75] Y. Zheng, Z. Zeng, P. Zou, L. Zhang, X. Li, P. Liu, R. Li, and Z. Xu, Phys. Rev. Lett. **103**, 043904 (2009).

[76] H.-W. Sun, P.-C. Huang, Y.-H. Tzeng, J.-T. Huang, C. D. Lin, C. Jin, and M.-C. Chen, Optica **4**, 976 (2017).

[77] C. Jin, X. Tang, B. Li, K. Wang, and C. D. Lin, Phys. Rev. Applied **14**, 014057 (2020).